



Controllable preparation of multishelled NiO hollow nanospheres via layer-by-layer self-assembly for supercapacitor application



Zeheng Yang ^{a,b}, Feifei Xu ^{a,b}, Weixin Zhang ^{a,b,*}, Zhousheng Mei ^{a,b}, Bo Pei ^{a,b}, Xiao Zhu ^{a,b}

^a School of Chemical Engineering, Hefei University of Technology, Hefei, Anhui 230009, PR China

^b Anhui Key Laboratory of Controllable Chemical Reaction & Material Chemical, Engineering, Hefei, Anhui 230009, PR China

HIGHLIGHTS

- Multishelled NiO hollow nanospheres were prepared via layer-by-layer self-assembly.
- Double-shelled NiO hollow nanospheres exhibit superior supercapacitive performance.
- Large surface area and porosity account for the excellent electrochemical properties.

ARTICLE INFO

Article history:

Received 2 May 2013

Received in revised form

5 July 2013

Accepted 14 July 2013

Available online 22 July 2013

Keywords:

Nickel oxide

Multishelled hollow nanosphere

Self-assembly

Hierarchical structure

Supercapacitor

ABSTRACT

In this work, we demonstrate a facile layer-by-layer (LBL) self-assembly method for controllable preparation of single-, double-, and triple-shelled NiO hollow nanospheres by calcining $\text{Ni(OH)}_2/\text{C}$ precursors formed at different stage. It is observed that the external nanoflakes of the NiO hollow nanospheres are inherited from the Ni(OH)_2 precursors organized on the surface of carbon spheres via a self-assembly growth process and the inner shells result from the formation of different Ni(OH)_2 layers within the carbon spheres during different preparation cycles. Supercapacitive performance of the three types of NiO hollow nanospheres as active electrode materials has been evaluated by cyclic voltammetry (CV) and galvanostatic charge–discharge. The results indicate that double-shelled NiO hollow nanosphere sample with largest surface area ($92.99 \text{ m}^2 \text{ g}^{-1}$) exhibits the best electrochemical properties among the three NiO hollow nanosphere samples. It delivers a high capacitance of 612.5 F g^{-1} at 0.5 A g^{-1} and demonstrates a superior long-term cyclic stability, with over 90% specific capacitance retention after 1000 charge–discharge cycles. This excellent performance is ascribed to the short diffusion path and large surface area of the unique hollow structure with nanoflake building blocks for bulk accessibility of faradaic reaction.

© 2013 Elsevier B.V. All rights reserved.

1. Introduction

With the rapid development of new energy storage systems, supercapacitors have attracted much interest because of their long life cycle and high power density [1–3]. Compared with electrical double layer capacitors (EDLC) operating in a double layer formed on the electrode surface, which may limit the specific capacitance and lead to lower energy density relative to their theoretical value, pseudocapacitors based on the oxidation–reduction reaction can provide 10–100 times higher capacitance, because the reaction not only takes place at the surface but also near the surface of the active electrode [4]. Transition metal oxides and conductive polymers are

frequently used as the Faradic redox pseudocapacitors [5]. Particularly, supercapacitors based on ruthenium oxide have shown ultra-high pseudocapacitance and excellent reversibility [6–8]. However, the high cost of ruthenium oxide makes this material unsuitable for commercial applications.

Alternatively, cost-effective nickel oxide (NiO) has been suggested as a promising electrode material due to its outstanding theoretical specific capacitance of 3750 F g^{-1} [9], high thermal stability, low toxicity and environmental impact [10,11]. However, comparatively low capacitance has been usually achieved in experiments due to its relatively poor electric conductivity and low accessible surface areas [12–14]. One of the solutions to the problems is to transform the materials from bulk forms into hierarchical, or hollow structures to increase their active surface areas and porosity for better mass transportation [11,15,16]. For examples, Li et al. reported the synthesis of network-like NiO hierarchical microspheres organized with ultrathin nanowires/nanosheets through a hydrothermal route, which

* Corresponding author. School of Chemical Engineering, Hefei University of Technology, Hefei, Anhui 230009, PR China. Tel./fax: +86 551 62901450.

E-mail address: wxzhang@hfut.edu.cn (W. Zhang).

exhibit maximum specific capacitance of 555 F g^{-1} at the current density of 2 A g^{-1} [15]. Meher et al. reported maximum specific capacitance of 420 F g^{-1} at the current density of 0.5 A g^{-1} for hierarchical porous NiO samples synthesized by a microwave assisted reflux method [16]. Ding et al. reported a template method to obtain the $\text{Ni}_2\text{CO}_3(\text{OH})_2$ nanosheets first on sulfonated polystyrene (sPS) hollow nanospheres and then to remove the sPS to produce NiO hollow nanospheres. A maximum specific capacitance of 570 F g^{-1} was displayed at the current density of 0.5 A g^{-1} [11].

As far as hollow structures, so far, various successful methods have been developed to achieve hollow structures, even those with complex structures, such as multishelled hollow spheres [17–24]. For example, multishelled hollow nanospheres of Cu_2O have been prepared by cetyltrimethylammonium bromide (CTAB) vesicle templating and an intermediate-templating phase transformation process [21]. Furthermore, Wang et al. present a templating process to prepare multishelled metal oxide hollow microspheres with carbonaceous microspheres as sacrificial templates, which were saturated with a metal nitrate solution beforehand and then heated in air for the evaporation of carbonaceous templates and the formation of metal oxide shells. The number of shells was controlled by the metal ion loading and the heating rate [22,23]. And they reported the enhancement of ethanol-sensing performance with increased number of the shells. Our group reported an inward replacement/etching route to synthesis of double-walled Cu_7S_4 nanoboxes by repeating formation of the Cu_7S_4 layer in Na_2S solution and dissolution of the Cu_2O core in ammonia solution for two consecutive cycles and found their enhanced performance in ammonia gas sensing in contrast with single-walled ones [24].

Inspired by these previous works, herein, we demonstrate controllable synthesis of single-, double-, and triple-shelled NiO hollow nanospheres with hierarchical structures. Different from the conventional immersion and calcination strategy, we adopt a stepwise immersion coupled with layer-by-layer (LBL) self-assembly method. That is, carbon spheres are periodically immersed in Ni^{2+} solution and followed by precipitation of $\text{Ni}(\text{OH})_2$ precursors in urea solution. And NiO hollow nanospheres are obtained through removing the carbon templates by heating subsequently. This modified approach has proven the following advantages. Firstly, self-assembly of $\text{Ni}(\text{OH})_2$ nanoflakes on carbon spheres during the precipitation process is beneficial to the preparation of the NiO hollow nanospheres with hierarchical structures. Secondly, the hollow nanospheres with designed number of shells can be easily obtained and are less affected by heating rate.

Moreover, supercapacitive performance of these different NiO hollow nanospheres with hierarchical structures has been evaluated by cyclic voltammetry (CV) and galvanostatic charge–discharge. The results show that these NiO hollow nanospheres exhibit high specific capacitance and good cycle performance. In particular, the double-shelled hollow nanospheres exhibit the best electrochemical properties among the three NiO hollow nanosphere samples.

2. Experimental section

In this work, all reagents were of analytical grade and used as received without further purification.

2.1. Preparation of multishelled NiO hollow nanosphere samples

Synthesis of carbon spheres: The carbon spheres were prepared as our previous report [25]. Typically, sucrose (13.86 g) was dissolved in distilled water (135 mL), and stirred with a magnetic stirrer to give a clear solution in a beaker. Then the solution was transferred into a Teflon-lined autoclave of 150 mL capacity, sealed and maintained at 190°C for 2 h. Then it was allowed to cool to

room temperature naturally. The black or brown products were collected by centrifugation, washed with ethanol and distilled water several times, and dried at 60°C for 12 h.

Synthesis of $\text{Ni}(\text{OH})_2/\text{C}$ precursors: Details of a typical experiment are as follows, carbon spheres (0.072 g) were dispersed in NiCl_2 solution (0.005 M, 40 mL) by ultrasonication for 0.5 h and stirring for 0.5 h to ensure that Ni^{2+} ions can be sufficiently adsorbed on the surface of carbon spheres. Then urea (0.25 g) was added and kept stirring for 0.5 h. Afterward, the mixture was transferred into a flask, sealed and maintained in a water bath at 90°C for 8 h. After that, the suspension was cooled to room temperature and centrifuged to obtain the $\text{Ni}(\text{OH})_2/\text{C}$ precursor of single-shelled NiO hollow nanospheres (named as S-NiO). For the precursor of double-shelled NiO hollow nanospheres (named as D-NiO) and triple-shelled NiO hollow nanospheres (named as T-NiO), the $\text{Ni}(\text{OH})_2/\text{C}$ precipitates were redispersed into the solution with the same concentration of NiCl_2 and urea again, and the preparation procedure was repeated by adsorbing Ni^{2+} ions and precipitating $\text{Ni}(\text{OH})_2$ in urea solution twice and three times, respectively. The as-obtained products were washed several times with distilled water and ethanol, and then dried at 60°C to get the corresponding $\text{Ni}(\text{OH})_2/\text{C}$ composites at different stages.

Synthesis of multishelled NiO hollow nanospheres: In order to prepare multishelled NiO hollow nanospheres, the $\text{Ni}(\text{OH})_2/\text{C}$ precursors obtained at different stage were heated to 450°C in air at the rate of 2°C min^{-1} , and kept at 450°C for 4 h. Then the furnace was gradually cooled to room temperature and single-, double-, and triple-shelled NiO hollow nanospheres were subsequently formed as the gray-powder products.

In addition, we prepared a comparison sample (named as C-NiO), which was obtained through the reaction of NiCl_2 and urea solution with the same concentration used in the synthesis of multishelled NiO hollow nanospheres in a water bath at 90°C for 8 h, followed by calcination at 450°C for 4 h.

2.2. Characterization of materials

The crystallographic characteristics of the samples were investigated by powder X-ray diffraction based on a Japan Rigaku D/max- $\gamma\beta$ X-ray diffractometer with $\text{Cu K}\alpha$ radiation ($\lambda = 0.15406 \text{ nm}$), operated at 40 kV and 80 mA. The morphologies and structures of the as-prepared samples were characterized by transmission electron microscopy (TEM) on a Hitachi H-800 transmission electron microscope at an accelerating voltage of 200 kV. Field emission scanning electron microscopy (FESEM) measurement was carried out with a field-emission microscope (FEI Sirion-200) operated at an acceleration voltage of 10 kV. The Brunauer–Emmett–Teller (BET) surface area and pore parameters of the samples were determined from nitrogen adsorption and desorption isotherms, measured at the temperature of liquid nitrogen on a NOVA 2200e surface area and pore size analyzer. Thermogravimetric (TG) analysis was carried out on a Netzsch TG209 F3 system at a rate of $10^\circ\text{C min}^{-1}$ from room temperature to 800°C in air. Raman spectra were collected at ambient temperature on a LABRHM-HR Raman spectrometer with an excitation wavelength of 514.5 nm.

2.3. Electrochemical measurements

The electrochemical measurements were performed on a CHI604C electrochemistry analyzer (Shanghai Chenhua Instrument Co., China) in a three-electrode system. The working electrode was prepared by mixing 70 wt% of the testing sample, 20 wt% acetylene black and 10 wt% polytetrafluoroethylene (PTFE) in ethanol and stirring to form slurry. Then it was coated on a nickel foam

substrate, and dried at 80 °C for 12 h under vacuum. The as-formed electrodes were then subjected to a pressure of 2 MPa. The active mass of the three samples coated on the nickel foam is in the range of 15–19 mg (S-NiO: 16 mg, D-NiO: 19 mg; T-NiO: 15 mg). All electrochemical measurements were carried out in 2 M KOH aqueous solution at room temperature using a Pt wire as the counter electrode and saturated calomel electrode (SCE) as the reference electrode. The specific capacitance of the electrode materials is calculated from the charge–discharge curves according to the following Equation (1):

$$C_m = I \times \Delta t / (\Delta V \times m) \quad (1)$$

where C_m (F/g) is the specific capacitance, I (A) is the current, Δt (s) is the discharge time of a cycle, ΔV (V) is the potential window, and m (g) is the mass of single electrode, respectively.

3. Results and discussion

The X-ray diffraction (XRD) patterns of single-, double- and triple-shelled NiO hollow nanospheres are shown in Fig. 1. The XRD patterns of the three samples could be indexed to cubic NiO (JCPDS No. 71-1179), and no obvious impurities, such as the precursor compounds have been detected. It can be seen that the intensity of the peaks for S-NiO, D-NiO and T-NiO is gradually increasing, indicating the increasing crystallinity with the progressive precipitation of the samples.

As the templates for synthesizing multishelled NiO hollow nanospheres, the structure of carbon spheres significantly affects the resulting products. The FESEM images of the carbon spheres obtained by hydrothermal carbonization of sucrose at 190 °C for 2 h are shown in Fig. S1 (Supporting information). It can be seen that the spheres have good dispersion and uniform size (average diameter of about 800 nm). The high-magnification image shows that the carbon spheres possess porous structures, as reported in our previous work [25]. These characteristics are beneficial to serve as templates for synthesizing multishelled hollow nanospheres subsequently.

The FESEM images of the Ni(OH)₂/C precursors harvested at different stage and the corresponding calcination products are shown in Fig. 2. As shown in Fig. 2A, the outside layer of the carbon spheres was assembled with the Ni(OH)₂ nanoparticles after the first preparation cycle. The as-formed Ni(OH)₂/C precursors have an average size of about 800 nm, which is similar to that of the carbon sphere templates. Single-shelled NiO hollow

nanospheres were obtained by calcining the precursors at 450 °C for 4 h in air (Fig. 2B). However, the diameter of S-NiO spheres is significantly reduced to about 300 nm due to the shrinkage of Ni(OH)₂/C precursors during the process of high temperature calcination, which is in agreement with previous report [26]. After the second preparation cycle, the formed Ni(OH)₂/C precursor spheres have an average size of about 1 μm due to assembly growth of loose Ni(OH)₂ nanoflakes on the surface (Fig. 2C). Double-shelled NiO hollow nanospheres (average size of about 700 nm) were obtained after heating treatment of the Ni(OH)₂/C precursor (Fig. 2D). Fig. 2E and F shows the images of the obtained Ni(OH)₂/C precursors after the third preparation cycle and the corresponding triple-shelled NiO hollow nanospheres obtained by subsequent heating, respectively. It can be seen that the Ni(OH)₂/C precursors have an average size of about 1 μm too, but the nanoflake building blocks on the shell of spheres become thicker and denser. Similarly, the resulting triple-shelled NiO hollow nanospheres have an average diameter of about 700 nm.

Fig. 3 shows the TEM micrographs of multishelled NiO hollow nanospheres. The single-, double- and triple-shelled structure of the products can be seen clearly from Fig. 3(A, B), (C, D) and (E, F), respectively. The shell of single-shelled NiO hollow nanospheres is mainly composed of small particles. For double-shelled NiO hollow nanospheres, loose nanoflakes build up its external shell and small particles construct the inner shell. Similar to this structure, triple-shelled NiO hollow nanospheres have an external shell assembled with nanoflakes, two inner shells organized with small particles. The FESEM images of S-NiO, D-NiO and T-NiO at high magnification are exhibited in Fig. S2. It can help us view the surface morphology of three samples clearly. The shell of S-NiO is assembled by nanoparticles with rough and porous structures. And the external shell of D-NiO is organized with loosely-packed, thin nanoflakes. Compared with D-NiO, the nanoflakes on the outside surface of T-NiO are becoming thicker and denser.

To characterize the specific surface area and porosity, nitrogen sorption measurements of the three samples were carried out at 77.4 K. Nitrogen adsorption/desorption isotherm of S-NiO, D-NiO, T-NiO samples and the corresponding Barrett–Joyner–Halenda (BJH) pore size distribution obtained from the desorption branch of the isotherm are shown in Fig. 4. All three isotherm profiles can be categorized to type IV with a small hysteresis loop observed in the relative pressure range of 0.7–0.95. The BJH pore size distribution curves indicate that there are abundant mesopores existing in these NiO samples [27].

Table 1 exhibits the results of the measured BET specific surface area and the BJH pore size distribution of the three samples. As shown in Table 1, S-NiO has a large specific surface area of 61.63 m² g⁻¹, D-NiO has the largest specific surface area of 92.99 m² g⁻¹, while T-NiO has the smallest specific surface area of 23.45 m² g⁻¹, which is ascribed to their structural difference. For S-NiO, the large surface area comes from the loose and porous shell. For D-NiO, the largest specific surface area results from the doubled-shelled hierarchical structure with assembly of loosely-packed, thin nanoflakes as external shells. However, for T-NiO, the thicker and densely-packed NiO nanoflakes on the external shells as well as the larger and densely-packed NiO particles on inner shells may reduce the specific surface area of the hollow nanospheres significantly, even though they have more shells. Moreover, three samples all have a porous structure, the average pore size of S-NiO, D-NiO and T-NiO is 18.24 nm, 7.04 nm and 12.30 nm, respectively. The ionic radius of OH⁻ in the electrolyte solution is 0.137 nm [28], thus, the three samples all have sufficient pore size to transport OH⁻ ions. Besides, D-NiO has the narrower pore size distribution than S-NiO and T-NiO, which will be more ideal as electrode material for supercapacitors because of its high

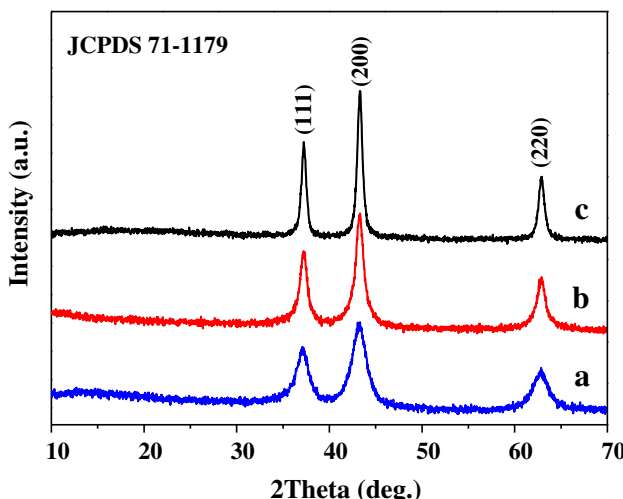


Fig. 1. XRD patterns of NiO hollow nanospheres. (a, S-NiO; b, D-NiO; c, T-NiO).

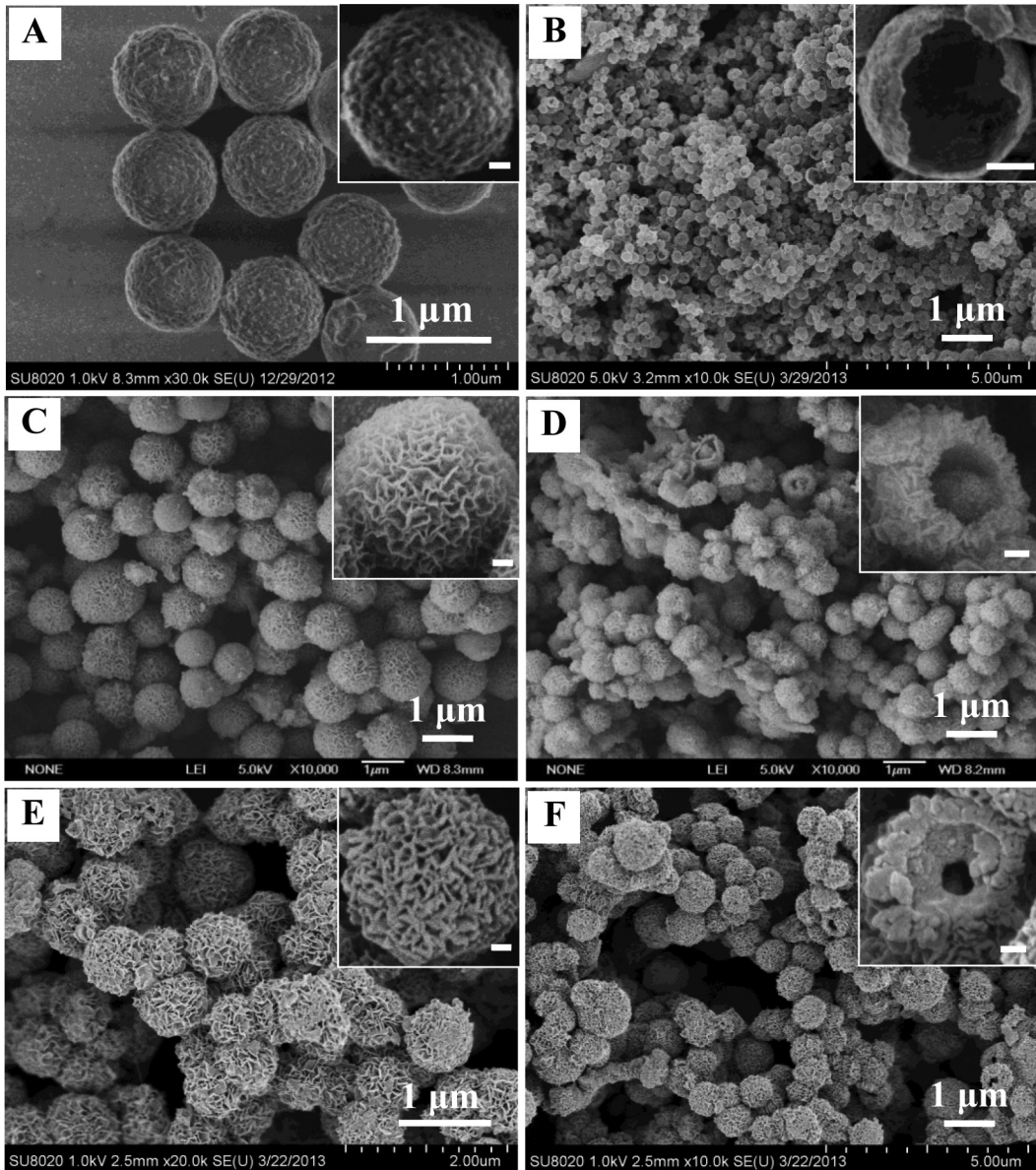


Fig. 2. FESEM images of the Ni(OH)₂/C precursors harvested at different stage and the corresponding calcination products. (A), (C), (E) the Ni(OH)₂/C precursors of S-NiO, D-NiO, T-NiO, respectively. (B) S-NiO; (D) D-NiO; (F) T-NiO. Insets: the corresponding high-magnification view. Scale bar: 100 nm.

specific surface area and narrow pore size distribution with many channels for diffusion of the electrolyte ions [29].

Single-, double-, and triple-shelled NiO hollow nanospheres were primarily synthesized by calcining the Ni(OH)₂/C precursors harvested at different stage in air. And these precursors were prepared via a layer-by-layer (LBL) self-assembly method, using the self-prepared carbon spheres as templates without any modification. Fig. 5 illustrates the major process steps in this study. Firstly, the negatively charged surface functional groups of carbon spheres, such as hydroxyl or carboxylic acid [22,23,26], attracted Ni²⁺ ions in NiCl₂ solution through adsorption. Secondly, urea was added in above solution and hydrolyzed to slowly release OH⁻ ions under heating at 90 °C, the OH⁻ ions reacted with Ni²⁺ ions to generate Ni(OH)₂. And the remaining negatively charged functional groups on or in the carbon spheres can promote further adsorption of Ni²⁺ ions again. This preparation cycle could be carried on once, twice and three times to obtain the Ni(OH)₂/C precursors of S-NiO, D-NiO and T-NiO, respectively.

During the first preparation cycle, crystal nucleation occurred after supersaturated solution with numerous Ni(OH)₂ mesocrystals was formed, which significantly decreased the concentration of Ni²⁺ ions in solution and accordingly restrained the further growth of the crystals. Consequently, only a thin layer of Ni(OH)₂ nanoparticles formed on and under the surface of carbon spheres and the Ni(OH)₂ nanoparticles inside carbon spheres could not assemble into nanoflakes because of the confinement within carbon spheres. And single-shelled NiO hollow nanospheres were obtained after removing the carbon templates through calcining in air. During the second preparation cycle, Ni²⁺ ions in solution were sequentially adsorbed on and in carbon spheres and during the second precipitation process, the initial Ni(OH)₂ precipitates provided nucleation centers to direct the growth and self-assembly of the external Ni(OH)₂ nanoflakes [30]. Afterward, thin Ni(OH)₂ nanoflakes were loosely built up on the surface of carbon spheres. However, nickel hydroxide inside carbon spheres could only exist in nanoparticles owing to confinement within carbon spheres, which

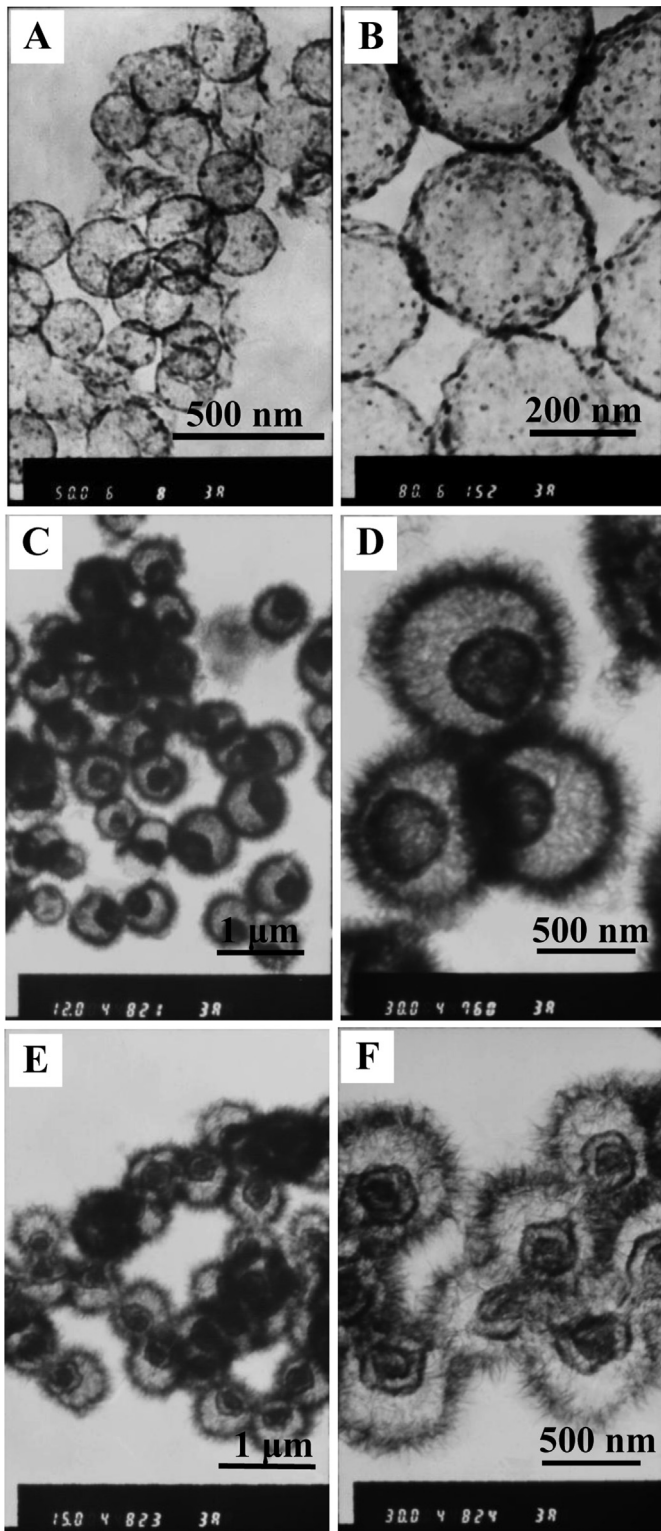


Fig. 3. TEM images of multishelled NiO hollow nanospheres. (A, B) S-NiO; (C, D) D-NiO; (E, F) T-NiO.

limited further assembly of these nanoparticles. During the third cycle, more and more Ni^{2+} ions were adsorbed on and in carbon spheres and the external Ni(OH)_2 nanoflakes continued to grow and became thicker and densely-packed through a ripening process. Similar to the second cycle, Ni(OH)_2 formed within carbon spheres took the format of nanoparticles due to the confinement.

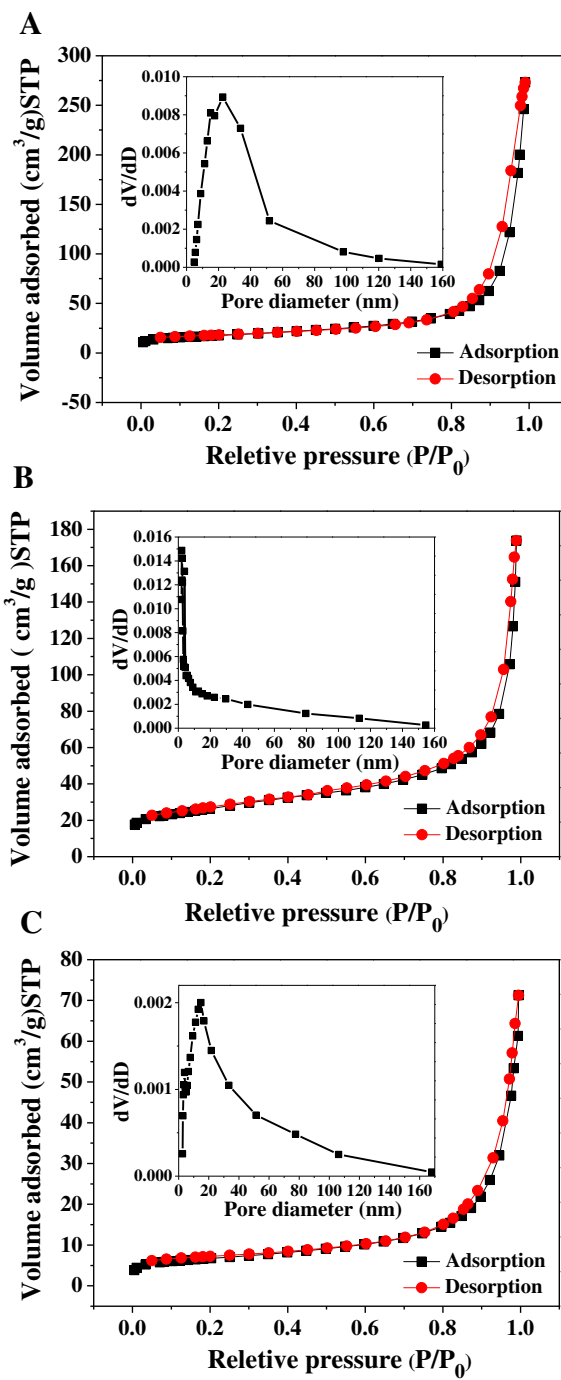


Fig. 4. Nitrogen adsorption–desorption isotherms of S-NiO (A); D-NiO (B); T-NiO (C). Insets: the corresponding BJH pore size distribution curves calculated from desorption branch.

Besides, there were interfaces existing between the Ni(OH)_2 layers formed in different preparation cycle due to their different penetration depth within the carbon spheres and crystallinity. The crystallinity of the $\text{Ni(OH)}_2/\text{C}$ precursors for S-NiO, D-NiO and T-NiO

Table 1

Surface and porosity characteristics of the three NiO samples.

Sample	BET surface area ($\text{m}^2 \text{ g}^{-1}$)	Average pore diameter (nm)
S-NiO	61.33	18.24
D-NiO	92.99	7.04
T-NiO	23.45	12.30

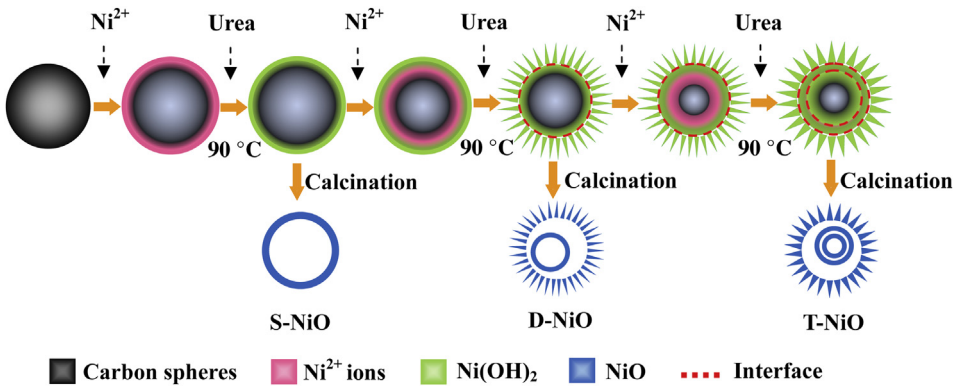


Fig. 5. Synthetic scheme of multishelled NiO hollow nanospheres via LBL self-assembly.

is gradually increasing with the progressive precipitation of the samples, which is shown in Fig. S3. When subjected to calcination in air, the $\text{Ni}(\text{OH})_2$ layers dehydrate and shrink to form nickel oxide shells and these nickel oxide shells were split from carbonaceous template in accordance with the order from the outer to the inner in the shrinking process of carbon spheres [22]. After removing carbonaceous templates, multishelled nickel oxide hollow nanospheres were formed.

We have done comparative experiments by changing the heating rate from $1\text{ }^{\circ}\text{C min}^{-1}$ – $3\text{ }^{\circ}\text{C min}^{-1}$ and interestingly found that the number of shells was decided by the preparation cycles and rarely affected by heating rate, which is different from the reported results [22,23].

The thermal behavior of the $\text{Ni}(\text{OH})_2/\text{C}$ precursors was studied by TGA to monitor the conversion process from $\text{Ni}(\text{OH})_2/\text{C}$ to NiO and determine the proper temperature for the removal of carbon spheres (Fig. S4). As shown in Fig. S4, most of the weight loss happened below $450\text{ }^{\circ}\text{C}$ for three samples, and after $450\text{ }^{\circ}\text{C}$, the weight loss is negligible compared with that before $450\text{ }^{\circ}\text{C}$. Furthermore, high calcination temperature could result in the formation of larger sized crystallites, which had negative effects on performance of supercapacitors [31]. So $450\text{ }^{\circ}\text{C}$ was chosen as the calcination temperature.

Furthermore, we also use Raman analysis to test S-NiO and D-NiO samples, and the results are shown in Fig. S5. Two main Raman peaks located at about 520 and 1090 cm^{-1} are observed in both spectra, corresponding to the shaking peaks of NiO . And the weak peaks located at 1550 cm^{-1} could be assigned to the shaking peaks of carbon [32]. However, in comparison with those of NiO , the intensity of the carbon peaks is very low, indicating that the carbon content in the products is quite low. So the effect of remnant carbon on the capacitance measured can be ignored.

We use the as-prepared materials to fabricate supercapacitor for investigating the electrochemical properties by carrying out cyclic voltammetry (CV) and galvanostatic charge–discharge measurements using a three-electrode cell system. Fig. 6 gives the CV curves of S-NiO, D-NiO and T-NiO at the scan rate of 5 mV s^{-1} , respectively, and implies that the capacitance of the material mainly results from the contribution of faradaic pseudo-capacitor caused by the fast and reversible redox reaction of NiO . Furthermore, it is apparent that the separation between leveled anodic and cathodic currents for D-NiO is the largest among the three samples at the same scan rate, while that of T-NiO is the smallest, meaning that D-NiO has the highest responding current and specific capacitance.

The rate performance for D-NiO is presented in Fig. 7A and B. Fig. 7A shows the CV curves of D-NiO at different scan rates. The anodic peak P1 results from the oxidation of NiO to NiOOH , and the cathodic peak P2 is due to the reverse reaction. The appearance of these redox peaks is involved in the following Equation (2):



With the increasing scan rate, the anodic peaks move toward higher potential and the cathodic peaks move toward lower potential at the same time, which may be attributed to the increasing electric polarization and irreversible reactions as the scan rate scales up [31]. Fig. 7B exhibits the charge–discharge curves of D-NiO at different current densities ($0.5, 1.0, 1.5, 2.0, 2.5$ and 3.0 A g^{-1}), performed between the potential range of 0 – 0.7 V in KOH aqueous solution (2 M). It can be seen that these charge–discharge curves exhibit good platforms, which further illustrate its pseudo-capacitance nature and are quite consistent with the result of CV curves in Fig. 7A. Correspondingly, the specific capacitances of D-NiO were $612.5, 555.4, 535.9, 520.8, 512.3$ and 509.4 F g^{-1} at $0.5, 1.0, 1.5, 2.0, 2.5$ and 3.0 A g^{-1} , respectively.

For comparison, the charge–discharge curves of S-NiO, T-NiO and C-NiO (comparison sample) were also measured and exhibited in Fig. S6. And the specific capacitances for these NiO electrodes calculated at different current densities were listed in Table 2. Obviously, the D-NiO electrode has higher specific capacitance of 612.5 F g^{-1} than the S-NiO (432.2 F g^{-1}), T-NiO (292.4 F g^{-1}) and C-NiO (184.7 F g^{-1}) electrodes. Its better electrochemical performance could be attributed to the larger surface area ($92.99\text{ m}^2\text{ g}^{-1}$) and the loosely-assembled thin nanoflakes of double-shelled NiO hollow nanospheres. The former can provide sufficient active surface area for bulk accessibility of faradaic reaction, and the latter is able to reduce the diffusion time of OH^- ions and ensures that most NiO building blocks could participate in the electrochemical reaction. Whereas, the lower specific capacitance of C-NiO electrode was

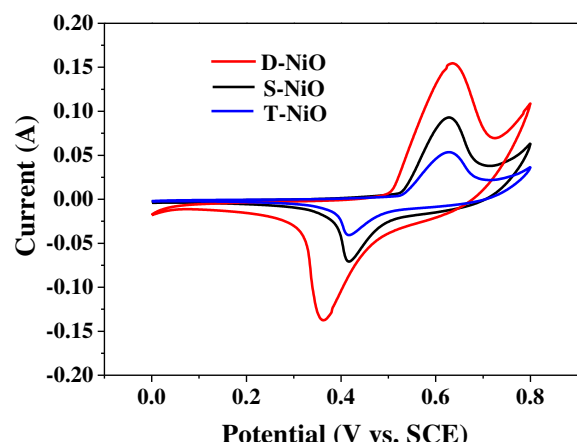


Fig. 6. Cyclic voltammograms of S-NiO, D-NiO and T-NiO at a scan rate of 5 mV s^{-1} .

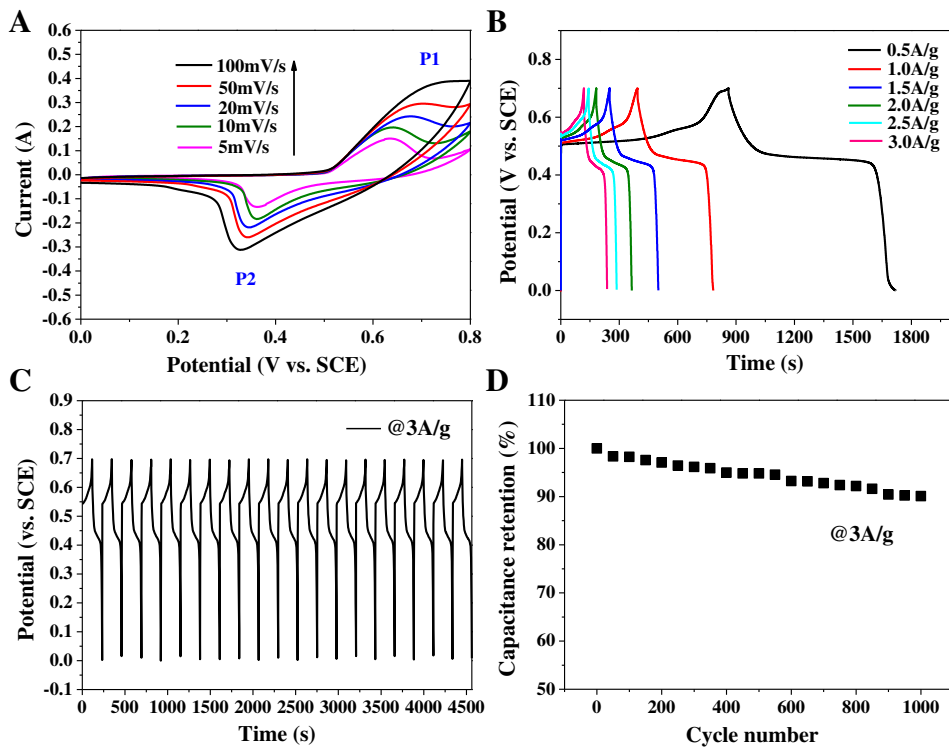


Fig. 7. (A) CV curves of D-NiO at different scan rates; (B) charge–discharge curves of D-NiO at different current densities; (C) galvanostatic charge–discharge curves of D-NiO at a current density of 3 A g^{-1} ; (D) average specific capacitance retention of D-NiO versus cycle number at a current density of 3 A g^{-1} .

Table 2

Specific capacitances of S-NiO, D-NiO, T-NiO and C-NiO electrodes at different current densities.

Sample	Specific capacitance (F g^{-1})					
	0.5 A g^{-1}	1 A g^{-1}	1.5 A g^{-1}	2 A g^{-1}	2.5 A g^{-1}	3 A g^{-1}
S-NiO	432.2	381.7	347.5	322.1	302.2	282.1
D-NiO	612.5	555.4	535.9	520.8	512.3	509.4
T-NiO	292.4	253.9	231.5	208.1	191.4	176.9
C-NiO	184.7	170.3	153.9	133.9	106.0	96.2

obtained probably because of its limited surface area for faradaic reaction and poor condition for the electrolyte ion diffusion (Fig. S7).

Considering that cycle stability is also a very important index to evaluate the supercapacitive performance of the materials, the

cycle performance for D-NiO was measured and is shown in Fig. 7C and D. Fig. 7C exhibits the charge/discharge curves of the first 20 cycles. It can be seen that the coulombic efficiency nearly reaches 100% for each cycle. Fig. 7D shows the specific capacitance retention versus cycle number at a current density of 3 A g^{-1} for D-NiO. It indicates that 90.1% of its initial capacitance can be retained after 1000 cycles, confirming the excellent cycling stability of D-NiO. The double-shelled hollow nanospheres with porosity can be beneficial to bulk active site accessibility and the diffusion of ions during the cycling process. Besides, the void space in the hollow nanospheres can effectively buffer the strain generated during the fast charging/discharging process, resulting in enhanced cycling performance [33]. These results demonstrate that such a hierarchical and hollow architecture is suitable for construction of supercapacitor electrodes with high electrochemical performance.

Typical Nyquist plots of the multishelled NiO hollow nanosphere electrodes measured in an open-circuit condition are presented in Fig. 8. At high-frequency, the point intersecting with the real axis exhibits an internal resistance, the internal resistances of S-NiO, D-NiO and T-NiO are about 0.57Ω , 0.54Ω and 0.60Ω . And the linear line at low-frequency delivers a Warburg impedance involved in the diffusion of electrolyte ions. For ideal supercapacitors, the impedance plot should be a line perpendicular to the real axis at low frequency. In our work, the slopes of straight lines are 64.3° , 76.8° and 48.8° for S-NiO, D-NiO and T-NiO. It can be seen that D-NiO electrode is much closer to ideal supercapacitors, proving its better capacitive behavior.

4. Conclusions

In summary, single-, double-, and triple-shelled NiO hollow nanospheres have been controllably prepared using a layer-by-layer (LBL) self-assembly method. The external nanoflakes of multi-shelled NiO hollow nanospheres are inherited from the Ni(OH)_2

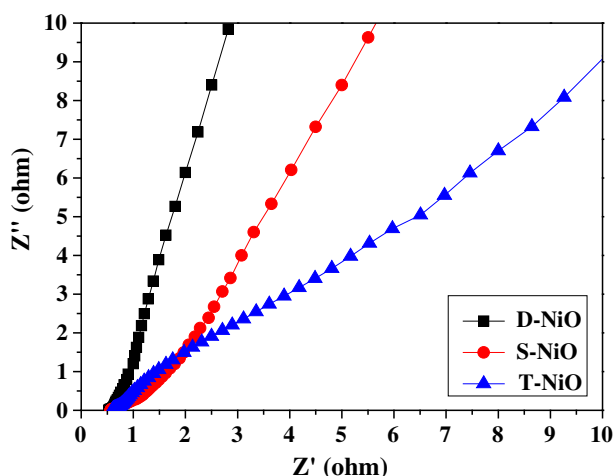


Fig. 8. Nyquist plots of the multishelled NiO hollow nanosphere electrodes.

precursors, which were organized on the surface of the carbon spheres via a self-assembly growth process. And the inner shells result from the formation of different Ni(OH)_2 layers within the carbon spheres during different preparation cycles, which were split from shrinking carbonaceous template under heating. The electrochemical measurements reveal that the double-shelled hollow nanospheres (D-NiO) with the large specific surface area ($92.99 \text{ m}^2 \text{ g}^{-1}$) have a higher specific capacitance of 612.5 F g^{-1} than S-NiO (432.2 F g^{-1}) and T-NiO (292.4 F g^{-1}) at 0.5 A g^{-1} . Furthermore, D-NiO also exhibits high capacitance retention of 90.1% after 1000 charge–discharge cycles. This excellent performance can be attributed to two factors. Firstly, larger active surface area of D-NiO can be beneficial for bulk accessibility of faradaic reactions. Secondly, the loosely-assembled, thin nanoflakes of D-NiO with porous structure provide short ion diffusion path for effective electrolyte diffusion. In short, further improvement of supercapacitive performance in faradaic-reaction-based electrode materials can be achieved by designing multishelled hollow structures with appropriate shells and self-assembled building blocks.

Acknowledgments

The authors are grateful to the financial supports of the National Natural Science Foundation of China (NSFC Grants 20976033, 21176054 and 21271058), the Fundamental Research Funds for the Central Universities (2010HGZY0012) and the Education Department of Anhui Provincial Government (TD200702).

Appendix A. Supplementary data

Supplementary data related to this article can be found at <http://dx.doi.org/10.1016/j.jpowsour.2013.07.057>.

References

- [1] R.B. Rakhi, W. Chen, D. Cha, H.N. Alshareef, *Nano Lett.* 12 (2012) 2559–2567.
- [2] P.C. Gao, A.H. Lu, W.C. Li, *J. Power Sources* 196 (2011) 4095–4101.
- [3] J. Yan, E. Khoo, A. Sumboja, P.S. Lee, *ACS Nano* 4 (2010) 4247–4255.
- [4] B.E. Conway, V. Birss, J. Wojtowicz, *J. Power Sources* 66 (1997) 1–14.
- [5] B. Wang, J.S. Chen, Z.Y. Wang, S. Madhavi, X.W. (David) Lou, *Adv. Energy Mater.* 2 (2012) 1188–1192.
- [6] J.W. Liu, J. Essner, J. Li, *Chem. Mater.* 22 (2010) 5022–5030.
- [7] M.N. Patel, X.Q. Wang, B. Wilson, D.A. Ferrer, S. Dai, K.J. Stevenson, K.P. Johnston, *J. Mater. Chem.* 20 (2010) 390–398.
- [8] G.P. Wang, L. Zhang, J.J. Zhang, *Chem. Soc. Rev.* 41 (2012) 797–828.
- [9] I.H. Kim, K.B. Kim, *J. Electrochem. Soc.* 153 (2006) A383–A389.
- [10] X.Y. Wang, X.Y. Wang, L.H. Yi, L. Liu, Y.Z. Dai, H. Wu, *J. Power Sources* 224 (2013) 317–323.
- [11] S.J. Ding, T. Zhu, J.S. Chen, Z.Y. Wang, C.L. Yuan, X.W. (David) Lou, *J. Mater. Chem.* 21 (2011) 6602–6606.
- [12] V.S.R. Channua, R. Holze, B. Rambabu, *Colloid Surf. A Physicochem. Eng. Asp.* 414 (2012) 204–208.
- [13] M.P. Yeager, D. Su, N.S. Marinkovic, X.W. Teng, *J. Electrochem. Soc.* 159 (2012) A1598–A1603.
- [14] Y.Z. Zheng, H.Y. Ding, M.L. Zhang, *Mater. Res. Bull.* 44 (2009) 403–407.
- [15] X.W. Li, S.L. Xiong, J.F. Li, J. Bai, Y.T. Qian, *J. Phys. Chem.* 22 (2012) 14276–14283.
- [16] S.K. Meher, P. Justin, G.R. Rao, *ACS Appl. Mater. Interfaces* 3 (2011) 2063–2073.
- [17] H.S. Qian, G.F. Lin, Y.X. Zhang, P. Gunawan, R. Xu, *Nanotechnology* 18 (2007) 355602.
- [18] H.X. Yang, J.F. Qian, Z.X. Chen, X.P. Ai, Y.L. Cao, *J. Phys. Chem. C* 111 (2007) 14067–14071.
- [19] X. Wang, X.L. Wu, Y.G. Guo, Y.T. Zhong, X.Q. Cao, Y. Ma, J.N. Yao, *Adv. Funct. Mater.* 20 (2010) 1680–1686.
- [20] H.G. Zhang, Q.S. Zhu, Y. Zhang, Y. Wang, L. Zhao, B. Yu, *Adv. Funct. Mater.* 17 (2007) 2766–2771.
- [21] H.L. Xu, W.Z. Wang, *Angew. Chem. Int. Ed.* 46 (2007) 1489–1492.
- [22] X.Y. Lai, J. Li, B.A. Korgel, Z.H. Dong, Z.M. Li, F.B. Su, J. Du, D. Wang, *Angew. Chem. Int. Ed.* 50 (2011) 2738–2741.
- [23] Z.H. Dong, X.Y. Lai, J.E. Halpert, N.L. Yang, L.X. Yi, J. Zhai, D. Wang, Z.Y. Tang, L. Jiang, *Adv. Mater.* 24 (2012) 1046–1049.
- [24] W.X. Zhang, Z.X. Chen, Z.H. Yang, *Phys. Chem. Chem. Phys.* 11 (2009) 6263–6268.
- [25] Z.H. Yang, Y.M. Pan, Z.S. Mei, W.X. Zhang, *Appl. Surf. Sci.* 258 (2012) 4756–4763.
- [26] X.M. Sun, Y.D. Li, *Angew. Chem. Int. Ed.* 43 (2004) 3828–3831.
- [27] M. Kruk, M. Jaroniec, *Chem. Mater.* 13 (2001) 3169–3183.
- [28] R.D. Shannon, *Acta Crystallogr. A* 32 (1976) 751–767.
- [29] J.W. Lee, T. Ahna, J.H. Kima, J.M. Kob, J.D. Kima, *Electrochim. Acta* 56 (2011) 4849–4857.
- [30] X.H. Xia, J.P. Tu, Y.Q. Zhang, X.L. Wang, C.D. Gu, X.B. Zhao, H.J. Fan, *ACS Nano* 6 (2012) 5531–5538.
- [31] L. Fan, L. Tang, H.F. Gong, Z.H. Yao, R. Guo, *J. Mater. Chem.* 22 (2012) 16376–16378.
- [32] Y. Jiang, D.D. Chen, J.S. Song, Z. Jiao, Q.L. Ma, H.J. Zhang, L.L. Cheng, B. Zhao, Y.L. Chu, *Electrochim. Acta* 91 (2013) 173–178.
- [33] C.Z. Yuan, X.G. Zhang, L.H. Su, B. Gao, L.F. Shen, *J. Mater. Chem.* 19 (2009) 5772–5777.